YOUNG STARLESS CORES EMBEDDED IN THE MAGNETICALLY DOMINATED PIPE NEBULA

P. Frau[1], J. M. Girart[1], M. T. Beltrán[2], O. Morata[3,4], J. M. Masqué[5],
G. Busquet[5], F. O. Alves[1], Á. Sánchez-Monge[5], R. Estalella[5] and G. A. P. Franco[6]

[1] Institut de Ciències de l'Espai (CSIC-IEEC), Campus UAB, Facultat de Ciències, Torre C-5p, 08193 Bellaterra, Catalunya, Spain
[2] INAF-Osservatorio Astrofisico di Arcetri, Largo Enrico Fermi 5, 50125 Firenze,Italy
[3] Institute of Astronomy and Astrophysics, Academia Sinica, P.O. Box 23-141, Taipei 106, Taiwan
[4] Department of Earth Sciences, National Taiwan Normal University, 88, Section 4, Ting-Chou Road, Taipei 11677, Taiwan.
[5] Departament d'Astronomia i Meteorologia and Institut de Ciències del Cosmos (IEEC-UB), Universitat de Barcelona, Martí i Franquès 1, 08028 Barcelona, Catalunya, Spain and
[6] Departamento de Física - ICEx - UFMG, Caixa Postal 702, 30.123-970, Belo Horizonte, Brazil

ABSTRACT

The Pipe Nebula is a massive, nearby dark molecular cloud with a low star-formation efficiency which makes it a good laboratory to study the very early stages of the star formation process. The Pipe Nebula is largely filamentary, and appears to be threaded by a uniform magnetic field at scales of few parsecs, perpendicular to its main axis. The field is only locally perturbed in a few regions, such as the only active cluster forming core B59. The aim of this study is to investigate primordial conditions in low-mass pre-stellar cores and how they relate to the local magnetic field in the cloud. We used the IRAM 30-m telescope to carry out a continuum and molecular survey at 3 and 1 mm of early- and late-time molecules toward four selected starless cores inside the Pipe Nebula. We found that the dust continuum emission maps trace better the densest regions than previous 2MASS extinction maps, while 2MASS extinction maps trace better the diffuse gas. The properties of the cores derived from dust emission show average radii of ∼0.09 pc, densities of $\sim 1.3 \times 10^5$ cm^{-3}, and core masses of ∼2.5 $M_\odot$. Our results confirm that the Pipe Nebula starless cores studied are in a very early evolutionary stage, and present a very young chemistry with different properties that allow us to propose an evolutionary sequence. All of the cores present early-time molecular emission, with CS detections toward all the sample. Two of them, Cores 40 and 109, present strong late-time molecular emission. There seems to be a correlation between the chemical evolutionary stage of the cores and the local magnetic properties that suggests that the evolution of the cores is ruled by a local competition between the magnetic energy and other mechanisms, such as turbulence.

Subject headings: ISM: individual objects: Pipe Nebula – ISM: lines and bands – ISM – stars: formation

1. INTRODUCTION

The Pipe Nebula is a massive (10^4 $M_\odot$: Onishi et al. 1999) filamentary (∼15 pc long and ∼3 pc wide) dark cloud located in the southern sky ∼5° apart from the Galactic Center. Its short distance to the Sun (145 pc: Alves & Franco 2007) places this complex in the group of nearby molecular clouds which serve as good laboratories for star formation surveys. Despite the large reservoir of mass, the Pipe Nebula molecular cloud is characterized by being apparently quiescent, with a very low star-formation efficiency (∼0.06% for the entire cloud, Forbrich et al. 2009). Barnard 59 (B59), located at the northwestern end of the cloud, has formed a small cluster of low-mass stars (Brooke et al. 2007). The low global star forming efficiency of the cloud contrasts with that of other nearby molecular clouds such as Ophiuchus or Taurus, where an important star-formation activity is observed. The Pipe Nebula is, hence, an excellent place to study the initial conditions of star formation at scales of a few parsecs.

The first extensive survey toward the Pipe Nebula was done by Onishi et al. (1999) through single dish observations of CO isotopologues. These authors were the first to suggest a clumpy distribution for the dense gas by detecting compact $C^{18}O$ cores in the main body of the cloud. It was not until the last few years that several surveys (Lombardi et al. 2006; Muench et al. 2007; Brooke et al. 2007; Rathborne et al. 2008; Lada et al. 2008) were carried out to explore the physical properties of the cloud. Lombardi et al. (2006) use 2MASS data to construct a high resolution extinction map of the Pipe Nebula through which

they identify a large number of high extinction cores with typical masses between 0.2 and 5 $M_\odot$. Molecular line observations reveal that they are starless cores in a very early evolutionary stage, associated with dense (10^4 cm^{-3}), relatively cold ($9.5 \le T_K \le 17$ K), and fairly quiescent gas (typical line widths of 0.4 km s^{-1}, Muench et al. 2007; Rathborne et al. 2008). Non-thermal gas motions inside the cores are subsonic and mass independent. Therefore, thermal pressure appears to be the dominant source of internal pressure. In addition, these cores appear to be pressure confined, but gravitationally unbound (Lada et al. 2008).

Recently, Alves et al. (2008) performed an optical polarimetric survey toward the diffuse gas in the Pipe Nebula. They find a large scale magnetic field that appears to be mostly perpendicular to the cloud main axis. The magnetic field exerts a pressure (∼10^6 K cm^{-3}) that is likely responsible for driving the collapse of the gas and dust cloud along the field lines. The polarization properties significantly change along the Pipe Nebula. This fact allowed the authors to distinguish three regions in the cloud: B59, the *stem*, and the *bowl* (see Fig. 1). B59 shows low polarization levels but high dispersion of the polarization position angles. Moving through the *stem* toward the *bowl*, the polarization level increases and the dispersion decreases. These authors propose that these three regions might be in different evolutionary stages. B59 is the only magnetically supercritical region and the most evolved of the Pipe Nebula, the *stem* would be at an earlier evolutionary stage, with material still collapsing, and finally, the *bowl* would be at the earliest stage, with cloud fragmentation just
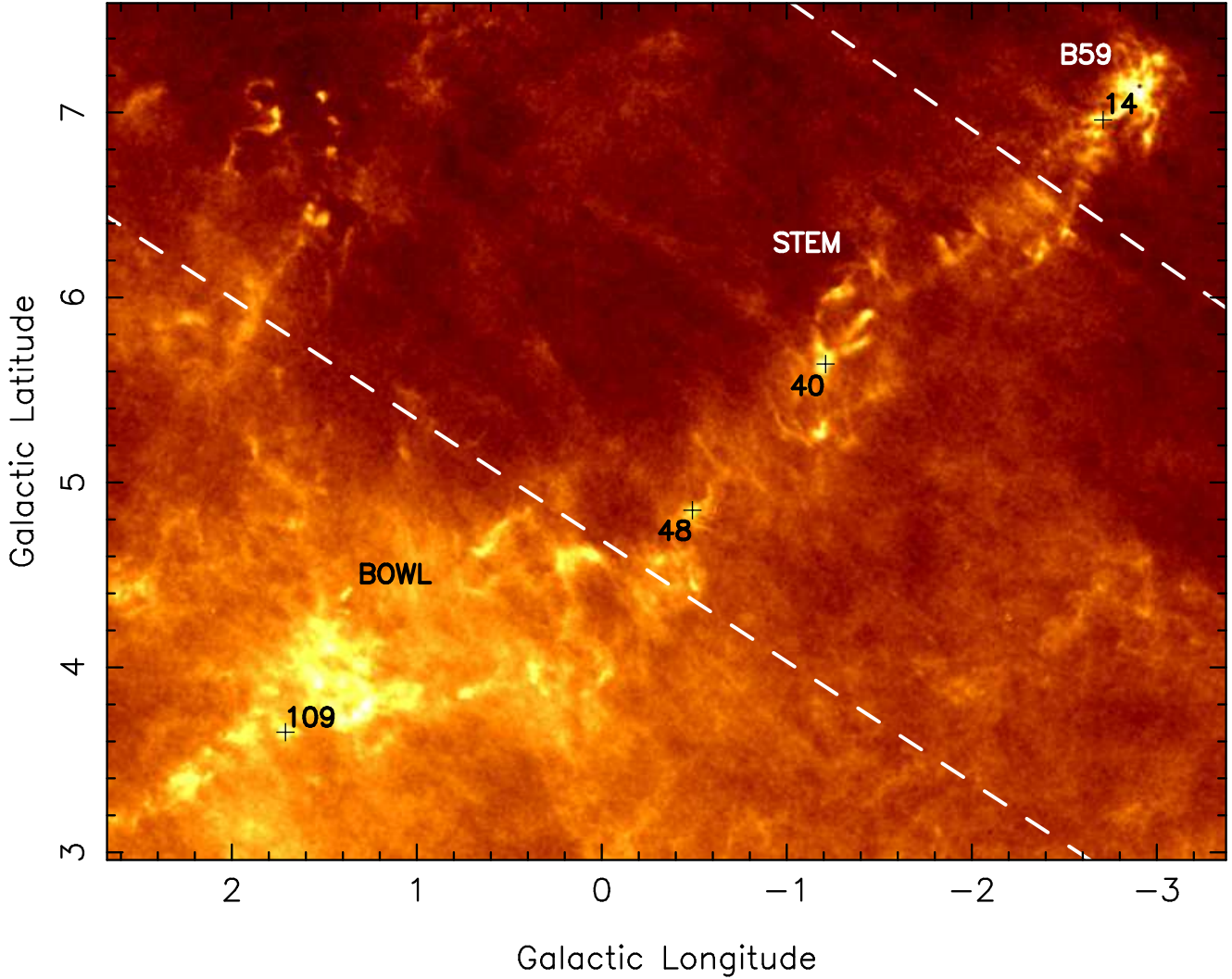
Frau et al.

Fig. 1.— Position of the observed cores plotted over the 2MASS extinction map of the Pipe Nebula (Lombardi et al, 2006). The dashed lines separate the three different magnetically defined regions (Alves et al. 2008). The lowest visual extinction (A_V) corresponds to 0.5 magnitudes. The highest A_V is observed toward the *bowl* of the Pipe and the B59 region, where it reaches approximately 20 magnitudes (Lombardi et al. 2006). We selected cores located in all three regions of the Pipe (*bowl*, *stem*, and B59).

TABLE 1
SOURCE LIST.

Source[a]	α(J2000) h m s	δ(J2000) ° ′ ″	v_{LSR} (km s^{-1})	Region[b]
Core 14	17 12 34.0	-27 21 16.2	+3.6	B59
Core 40	17 21 16.4	-26 52 56.7	+3.3	*Stem*
Core 48	17 25 59.0	-26 44 11.8	+3.6	*Stem*
Core 109	17 35 48.5	-25 33 05.8	+5.8	*Bowl*

(a) According to Lombardi et al. (2006) numbering.
(b) According to Alves et al. (2008) diffuse gas polarimetric properties.

started.

Based on Alves et al. (2008) results, we selected a sample of cores distributed in the different regions of the Pipe Nebula. We started an extensive molecular survey of these cores using the IRAM 30-m telescope. The aim of this study is to probe their chemical evolutionary stage, which could be related with the dynamical age according to chemical modeling of starless cores (Taylor et al. 1998; Morata et al. 2003; Tafalla et al. 2006). These models predict that some molecules, such as carbon-containing molecules, are formed very early in the chemical evolution, and are known as early-time molecules. These species are expected to be abundant in chemically young or low density cores, and most of them seem to be affected earlier by depletion effects (see e.g., Taylor et al. 1998; Ohashi et al. 1999; Bergin et al. 2001; Tafalla et al. 2006). Other species, such as nitrogen-bearing molecules and deuterated species, require a longer time to form. Thus, they are formed later in the chemical evolution and are known as late-time molecules. They are not expected to be depleted until densities of 10^6 cm^{-3} are reached (see e.g. Caselli et al. 2002; Flower et al. 2006; Bergin & Tafalla 2007; Aikawa et al. 2008). The qualitative comparison of the relative abundances of different types of molecules in each core can provide us with some clues about their possible evolutionary stage. From the observational point of view, there have been several authors that have studied the evolutionary stage of pre- and protostellar cores through molecular surveys. For instance, Kontinen et al. (2000) have used a large sample of molecules in a prestellar and a protostellar core. They find very different chemical compositions, specially in N_2H^+ and long carbon-chain molecule abundances. The former is typical of a pure gas-phase chemistry, while the latter require an evolved chemistry to form. According to time-

dependent chemistry models they interpret the differences as different stages of chemical evolution. Later, Tafalla et al. (2004) made a chemical analysis of L1521E, which helped to determine the extreme youth of this prestellar core. From the theoretical point of view, Aikawa et al. (2003) have simulated the evolution of a prestellar core and identified the different molecular abundances at different evolutionary stages to finally compare the results with the sample of Tafalla et al. (2002). Morata et al. (2003, 2005) have used the modeling results of Taylor et al. (1998) to compare with observations toward the L673 molecular cloud.

Based on this, we observed a set of early- and late-time molecules (see Table 2) toward the selected cores for a subsequent comparison. In addition, we mapped the 1.2 mm dust continuum emission of the cores to obtain a complete description of the structure, chemistry and evolutionary stage of the four selected Pipe Nebula cores.

2. OBSERVATIONS AND DATA REDUCTION

2.1. *MAMBO-II observations*

We mapped the Cores 14, 40, 48, and 109 (according to the Lombardi et al. 2006 numbering) at 1.2 mm with the 117-receiver MAMBO-II bolometer (array diameter of $240''$) of the 30-m IRAM telescope in Granada (Spain). The positions and velocity of the local standard of rest (v_{LSR}) for each core are listed in Table 1. The observations were carried out in April and May 2009 and in January and March 2010, in the framework of a flexible observing pool. A total of 13 usable maps were selected for analysis: 3 for Cores 14, 40, and 109, and 4 for Core 48. The weather conditions were good, with zenith optical depths between 0.1 and 0.3 for most of the time. The maps were taken at an elevation of $\lesssim 25°$ due to the declination of the sources.

The beam size of the telescope is $\sim 11''$ at the effective frequency of 250 GHz. The sources were observed with the on-the-fly technique, with the secondary chopping between $46''$ and $72''$ parallel to the scanning direction of the telescope. The telescope was constantly scanning at a speed of $8''$ s^{-1} for up to 65 s. This resulted in typical integration times for each map of ~1 hour. When possible, each source was mapped with different scanning directions (in equatorial coordinates) or rotating the secondary mirror of the telescope to avoid scanning artifacts in the final maps. We measured the zenith optical depth with a skydip and checked pointing and focus before and after each map. The average corrections for pointing and focus stayed below $3''$ and 0.2 mm, respectively. Flux density calibrators were observed every few hours.

The data were reduced using MOPSIC with the iterative reduction strategy developed by Kauffmann et al. (2008). The main advantages of the new scheme are that (*i*) sources much larger than in the classical approach can be recovered, (*ii*) the signal-to-noise ratio (SNR) of the final map increases, and (*iii*) they suffer from less artifacts. The figures were created using the GREG package, from the GILDAS[1] software.

All the maps have been convolved with a $21''.5$ Gaussian, larger than the telescope beam, in order to improve the SNR, and to smooth the appearance of the maps. The size of the Gaussian was chosen to be the one of the CN (1–0) molecular transition (see Table 2) which provides good spatial resolution and large SNR for the four maps.

[1] MOPSIC and GILDAS data reduction packages are available at http://www.iram.fr/IRAMFR/GILDAS

TABLE 2
MOLECULAR TRANSITIONS OBSERVED TOWARD THE PIPE NEBULA CORES WITH THE
IRAM 30-M ANTENNA.

Molecule	Transition	Frequency (GHz)	Beam ($''$)	Beam efficiency[a]	Δv [b] (km s^{-1})	Type[c]
C_3H_2	$(2_{1,2}-1_{1,0})$	85.3389	29.0	0.78/0.81	0.07	E
HCN	(1–0)	88.6318	28.0	0.78/-	0.07	E
N_2H^+	(1–0)	93.1762	26.5	0.77/0.81	0.06	L
$C^{34}S$	(2–1)	96.4130	26.0	-/0.81	0.06	E
CS	(2–1)	97.9809	25.5	0.76/0.81	0.06	E
CN	(1–0)	113.4909	21.5	0.75/0.81	0.05	E
N_2D^+	(2–1)	154.2170	15.0	0.77/0.74	0.04	L
DCO^+	(3–2)	216.1126	10.5	0.57/0.63	0.03	L
CN	(2–1)	226.8747	10.0	0.53/0.63	0.03	E
N_2D^+	(3–2)	231.3216	10.0	0.67/0.63	0.03	L
$H^{13}CO^+$	(3–2)	260.2554	9.0	0.53/0.63	0.02	L

(a) ABCD and EMIR receiver, respectively
(b) Spectral resolution.
(c) E = Early-time. L = Late-time. See §1 and §4.3 for details.

2.2. *Line observations*

We made several pointed observations within the regions of the Cores 14, 40, 48, and 109 with the heterodyne receivers of the 30-m IRAM telescope (ABCD and EMIR receivers). The observations were carried out in three epochs. The first epoch was August and September 2008. We used the capability of the telescope to perform simultaneous observations at different frequencies to observe the emission of the C_3H_2 $(2_{1,2}-1_{1,0})$, HCN (1–0), N_2H^+ (1–0), CS (2–1), CN (1–0), N_2D^+ (2–1), DCO^+ (3–2), CN (2–1), N_2D^+ (3–2) and $H^{13}CO^+$ (3–2) molecular transitions arranged in 3 different frequency setups covering the 3, 2, 1.3 and 1.1 mm bands. To do this, we combined the A100/B100/A230/B230 and A100/D150/A230/D270 SIS heterodyne receivers. The observational strategy was first to observe several positions with a $20''$ spacing centered on the $C^{18}O$ pointing center reported by Muench et al. (2007) (depicted by star symbols in Fig. 2), which is very close to the visual extinction peak position of each core (Lombardi et al. 2006). The visual extinction peak is assumed to be the densest region of the core, and it was defined as core center by Muench et al. (2007). The second and third epochs were August 2009 and June 2010, respectively, both using the new EMIR E0/E1/E2 receivers. We observed deeper toward the position of the grid of first epoch closer to the dust continuum peak (see circle symbols in Fig. 2). We observed also the $C^{34}S$ (2–1) molecular transition. Table 2 shows the transitions and frequencies observed. We used the VESPA autocorrelator as the spectral backend, selecting a channel resolution of 20 kHz, which provided a total bandwidth of 40 MHz. The corresponding velocity resolutions, main-beam efficiencies and half-power beam widths at all the observed frequencies are also listed in Table 2. We used the frequency-switching mode with a frequency throw between 3.83 and 22.98 MHz, depending on the transition. System temperatures in nights considered "good" were between 200 to 275 K at 3 mm, and between 440 and 960 K at 1 mm (T_{sys} reached 450 K and 3200 K in bad nights, respectively). Pointing was checked every 2 hours.

We reduced the data using the CLASS package of the GILDAS[1] software. We obtained the line parameters either from a Gaussian fit or from calculating their statistical moments when the profile was not Gaussian.

3. RESULTS AND ANALYSIS
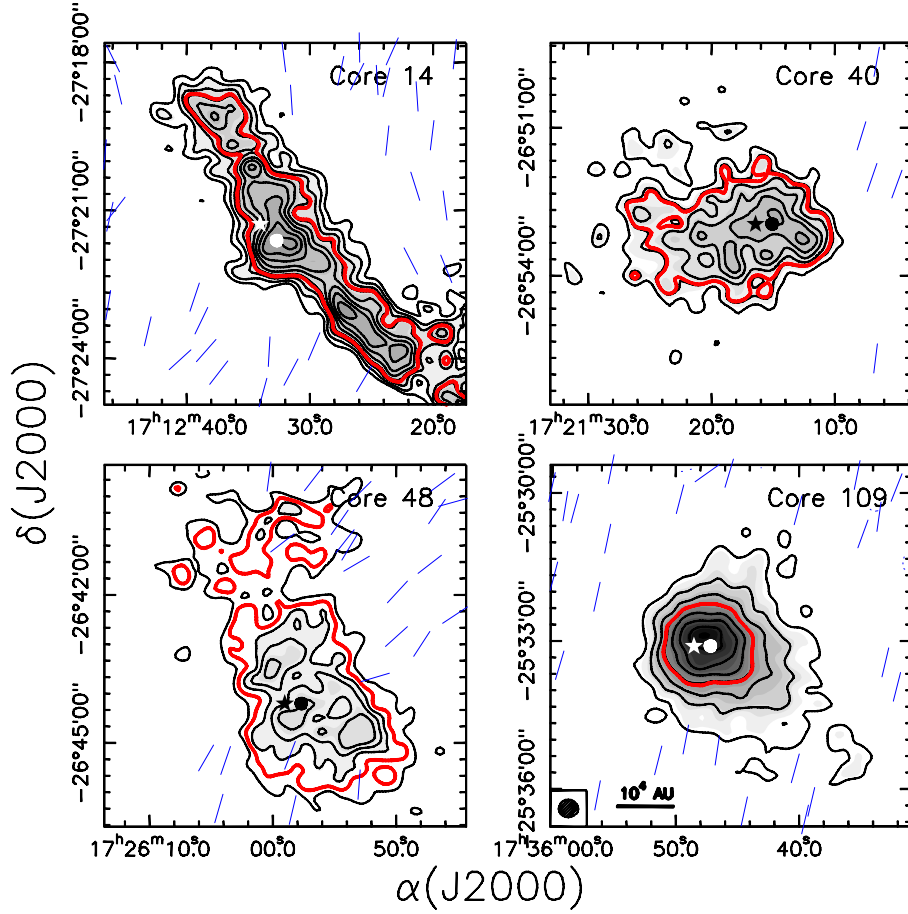
3.1. *Dust continuum emission*

FIG. 2.— IRAM 30-m MAMBO-II maps of the dust continuum emission at 1.2 mm toward four cores of the Pipe Nebula. The greyscale levels for all the maps are 3 to 18 times 5.75 mJy beam^{-1}. The contour levels are 3 to 11 times σ in steps of 1-σ, for Cores 14, 40 and 48, and 3 to 21 σ in steps of 3-σ for Core 109. 1-σ is 4.5, 5.0, 3.5, and 4.5 mJy beam^{-1} for Core 14, 40, 48, and 109, respectively. The red thick contour mark the half maximum emission level of the source (see Table 3). Black or white stars indicate the C^{18}O pointing center reported by Muench et al. (2007), which is very close to the visual extinction peak position of each core (Lombardi et al. 2006). Black or white filled circles indicate the position where line observations have been performed, close to the dust continuum emission maximum which falls into the beam area. The blue vectors depict the magnetic field vector found by Franco et al. (2010). Note that for Core 40 there are no optical polarimetry measurements on the east side due to the high visual extinction. In the bottom left corner of the bottom right panel the convolved beam and the spatial scale for the maps is shown.

TABLE 3
1.2 MM CONTINUUM EMISSION PARAMETERS.

Source	α(J2000) [a] h m s	δ(J2000) [a] $\circ\,'\,''$	T_{dust} (K)	RMS (mJy beam^{-1})	S_ν (Jy)	I_ν^{Peak} (mJy beam^{-1})	Diameter (pc)	N_{H_2} [b] (10^{21}cm^{-2})	n_{H_2} [b] (10^4cm^{-3})	Mass [b] ($M_\odot$)
Core 14 (filament)	17 12 31.5	−27 21 41.0	12.0[c]	4.5	2.56	51.6	0.106	12.21	5.59	2.87
Core 14 (core)					1.24		0.071	13.27	9.09	1.40
Core 40	17 21 14.7	−26 52 47.8	10.3[c]	5.0	1.73	42.0	0.104	11.05	5.16	2.51
Core 48	17 25 57.3	−26 44 22.3	10.0[d]	3.5	1.44	27.9	0.127	6.14[d]	2.35[d]	2.09[d]
Core 109	17 35 47.7	−25 32 52.9	9.5[c]	4.5	2.76	105.3	0.063	47.60	36.57	4.00

(a) Pointing position of the chemical observations which lies inside the same beam area of the dust continuum emission peak.
(b) Assuming $\kappa_{250\ GHz}$=0.0066 cm^2 g^{-1} as a medium value between dust grains with thin and thick ice mantles (Ossenkopf & Henning 1994). See Appendix A for details on the calculation.
(c) Adopted to be equal to the kinetic temperature derived for NH$_3$ (Rathborne et al. 2008).
(d) No kinetic temperature estimate, therefore we assumed 10 K based on the temperatures of the other cores (Rathborne et al. 2008).

TABLE 4
H_2 COLUMN DENSITIES[a], N_{H_2}, OF THE PIPE NEBULA CORES IN CM^{-2}.

Source	10.″5	15.″0	21.″5	27.″0
Core 14	1.75×10^{22}	1.38×10^{22}	1.21×10^{22}	1.11×10^{22}
Core 40	1.32×10^{22}	1.28×10^{22}	1.12×10^{22}	1.07×10^{22}
Core 48	1.09×10^{22}	8.88×10^{21}	7.38×10^{21}	6.99×10^{21}
Core 109	4.19×10^{22}	3.73×10^{22}	3.23×10^{22}	3.08×10^{22}

(a) Average column densities are calculated within one beam area toward the dust continuum emission peak. The values of $\kappa_{250 GHz}$ and T_{dust} are the same as for Table 3. These values are combined with the molecular column densities to find the molecular abundances in the same beam area. The correspondence is: 10.″5 with DCO$^+$, 15.″0 with N$_2$D$^+$, 21.″5 with CN (1–0) and, finally, 27.″0 with C$_3$H$_2$, HCN, N$_2$H$^+$, CS and C^{34}S.

In Fig. 2 we present the MAMBO-II maps of the dust continuum emission at 1.2 mm toward the four selected cores of the Pipe Nebula, convolved to a 21.″5 beam. Table 3 gives the peak position of the 1.2 mm emission after convolution with a Gaussian, the dust temperature (Rathborne et al. 2008), the RMS noise of the emission, the flux density and the value of the emission peak. Additionally, we also give the derived FWHM equivalent diameter, which is the diameter of the circular area equal to the area within the FWHM level, depicted by a red contour in Fig. 2. Table 3 also lists the H$_2$ column and volume density, as well as the mass for each core. These parameters are derived from the emission within the 3-σ level and discussed in §4.

The flux density of the cores ranges between ∼1.24 and ∼2.76 Jy. Note, however, that the extinction maps show that the studied cores are surrounded by a diffuse medium (see Fig. 1 and Lombardi et al. 2006). The on-the-fly reduction algorithms assume that the map limits have a zero emission level. Due to the presence of the diffuse material, this could not be true for the observed cores, and, therefore, the measured flux density of the maps might be lower than the actual value. We derived average H$_2$ column densities (N_{H_2}, see Appendix A) toward the dust continuum emission peak for the different resolutions (listed in Table 4) of the detected molecular transitions (see Table 5). We derived their abundances with respect to H$_2$. The results are discussed in § 4.

The maps of Fig. 2 show the different morphology of the cores. Following the results of Alves et al. (2008), it is interesting to compare the shape of the cores with their location along the Pipe Nebula. Core 14, located in B59, belongs to a clumpy and filamentary structure of ∼500″ (∼0.35 pc) elongated along the NE-SW direction. This is in perfect agreement with previous extinction maps (Lombardi et al. 2006; Román-Zúñiga et al. 2009). On the other hand, Core 109, located in the *bowl*, shows a compact and circular morphology with a FWHM of ∼90″ (∼0.063 pc). Cores 40 and 48, both located in the *stem*, have elliptical morphologies with extended diffuse emission.

3.2. *Molecular survey of high density tracers*

Muench et al. (2007) reported C^{18}O pointed observations toward the Pipe Nebula cores measured with a resolution of 56″. As seen in their Fig. 1, the position of the C^{18}O is very close to the visual extinction peak position of each core (Lombardi et al. 2006). Our higher resolution maps show a peak position offset for all the cores. As listed in Tables 1 and 3, and as shown in Fig. 2, the dust continuum peak does not coincide exactly with the A_V peak (stars in Fig. 2). However, the difference is compatible with the angular resolution
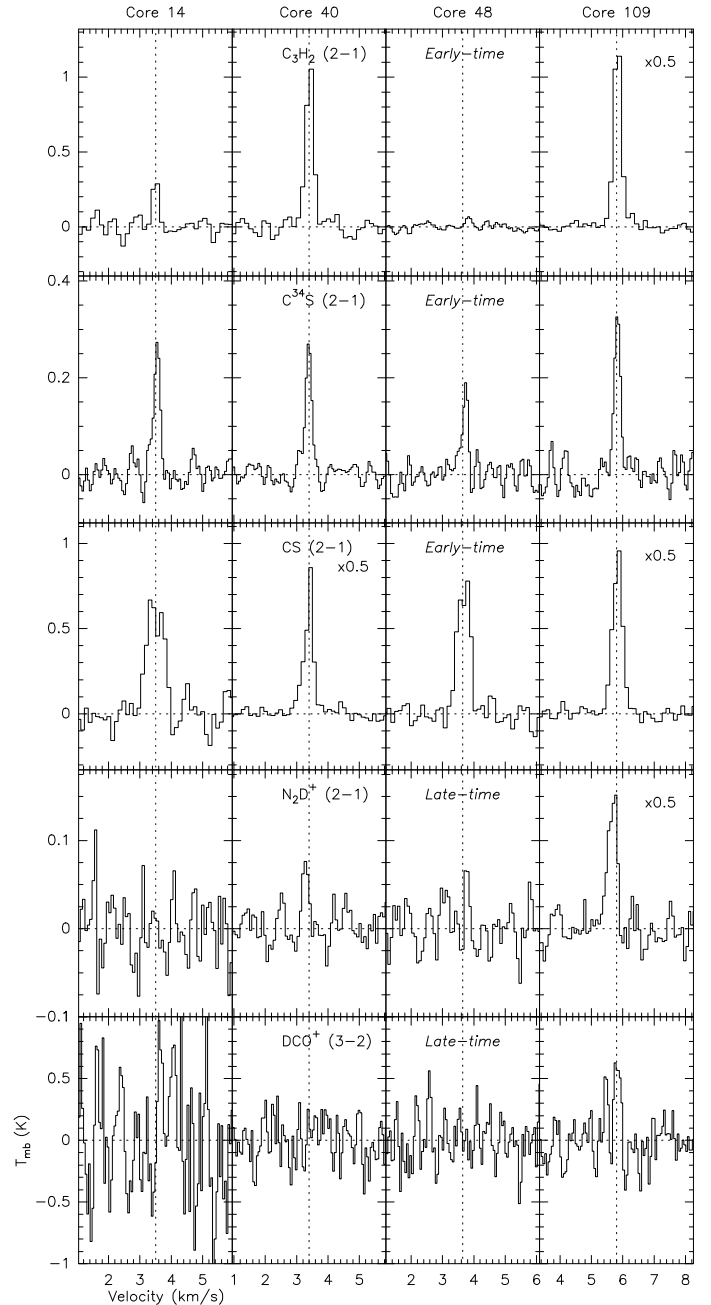

FIG. 3.— IRAM 30-m line spectra of the molecular transitions with no hyperfine components toward the four selected cores of the Pipe Nebula (see Table 1). The name of the core is indicated above the top panel of each column. Rows correspond to a single molecular transition specified on the second column. The velocity range is 5 km s^{-1}, and it is centered on the v_{LSR} of each core is marked with a vertical dotted line. Vertical axis show the T_{MB} of the emission, and the zero level is marked by a horizontal dotted line. Some of the Core 109 spectra, with the highest measured T_{MB}, have been divided by 2 to fit to the common scale.

of the extinction maps. We decided to present only molecular line data of the observed positions closer to the dust continuum emission peak (circles in Fig. 2), defined as the core center and supposed to exhibit brighter emission from molecular transitions. The typical core size is ∼90″ or larger (see Table 3). The beam size of the detected lines, except for N$_2$D$^+$ (2–1) and DCO$^+$ (3–2), range from 21.″5 to 29.″0, while the initial grid of pointed position had a separation of 20.″0, thus the emission peak stays within the beam area for
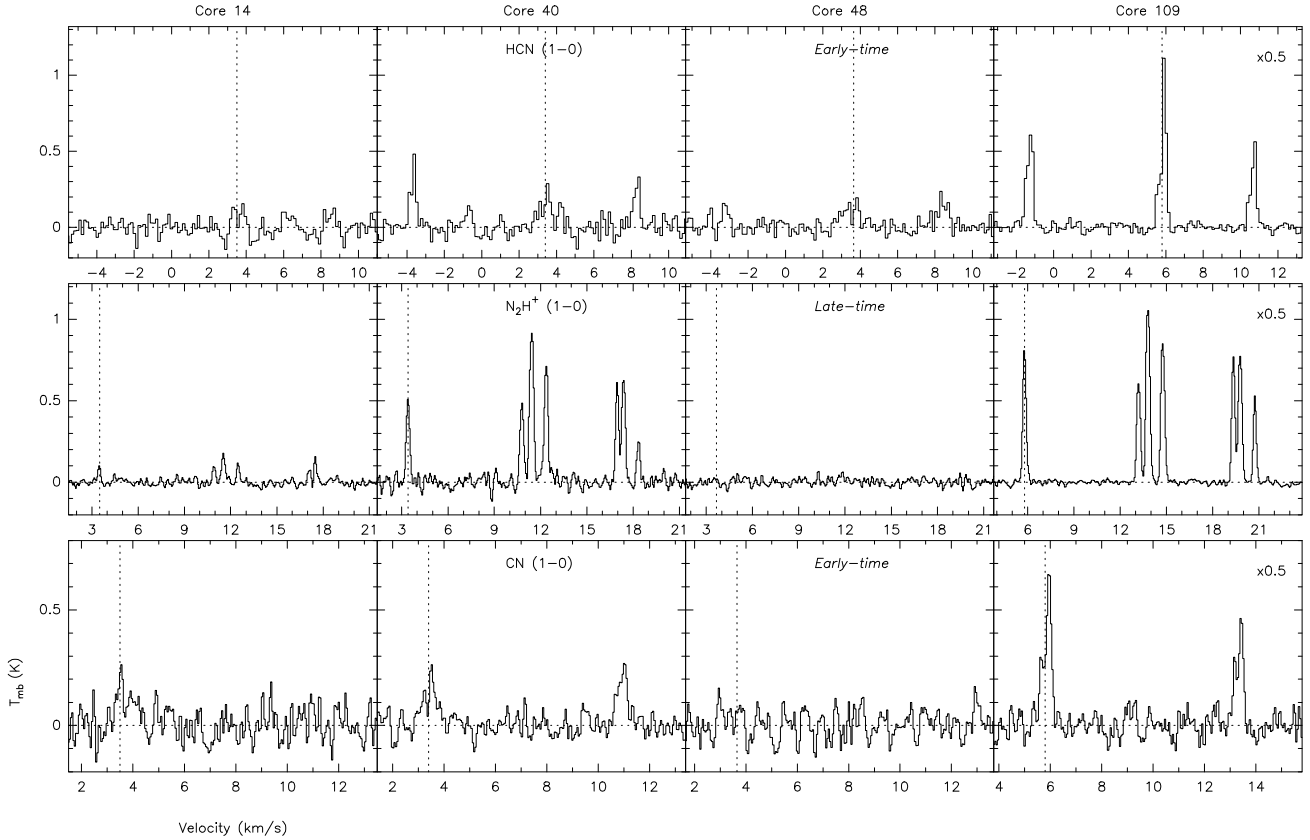
FIG. 4.— IRAM 30-m line spectra of the molecular transitions with hyperfine components toward the four selected cores of the Pipe Nebula (see Table 1). The name of the core is indicated above the top panel of each column. Rows correspond to a single molecular transition specified on the second column. The velocity range is 16.5, 20 and 12 km s^{-1} for HCN (1–0), N$_2$H$^+$ (1–0) and CN (1–0) respectively. The v_{LSR} of each core is marked with a vertical dotted line. Vertical axis show the T_{MB} of the emission, and the zero level is marked by a horizontal dotted line. Core 109 spectra, with the highest measured T_{MB}, have been divided by 2 to fit to the common scale.

TABLE 5
SUMMARY OF DETECTIONS AND UPPER LEVELS IN K TOWARD THE PIPE NEBULA
CORES^a.

Molecular	Core			
transitions	14	40	48	109
C$_3$H$_2$ (2$_{1,2}$–1$_{1,0}$)	√	√	<0.07	√
HCN (1–0)	<0.21	√	√	√
N$_2$H$^+$ (1–0)	√	√	<0.07	√
C^{34}S (2–1)	√	√	√	√
CS (2–1)	√	√	√	√
CN (1–0)	√	√	<0.17	√
N$_2$D$^+$ (2–1)	<0.12	√	<0.08	√
DCO$^+$ (3–2)	<1.71	<0.61	<0.76	√
CN (2–1)	<0.97	<1.70	<0.76	<0.90
N$_2$D$^+$ (3–2)	<1.01	<0.93	<1.94	<0.91
H^{13}CO$^+$ (3–2)	<1.52	<1.40	<2.38	<1.34

(a) The transitions marked with √ have been detected toward the corresponding core. Otherwise, the 3σ upper limit is shown.

these molecular transitions. Therefore, the molecular line properties that we obtain are representative of the chemistry of the core center.

Table 5 summarizes the detections or the 3σ upper limits of the non detections toward each core. Table 6 give the parameters of the detected lines. In Figs. 3 and 4 we show the spectra of the different molecular transitions observed toward the dust continuum emission peak of each core. Core 109 shows the stronger emission in all the detected transitions in our sample. This is the core with the most compact and circular morphology (see Fig. 2). Core 40 shows also emission in the six

molecular transitions at 3 mm (C$_3$H$_2$ (2$_{1,2}$–1$_{1,0}$), HCN (1–0), N$_2$H$^+$ (1–0), C^{34}S (2–1), CS (2–1), and CN (1–0)), although their intensities are lower than for Core 109. Core 14 shows emission in all the 3 mm transitions except in HCN (1–0). Finally, Core 48 only shows emission in CS (2–1), C^{34}S (2–1), and HCN (1–0).

In addition to the line parameters, we derived the molecular column densities for all the detected species (see Appendix B for details) which are listed in Table 7. For the transitions with detected hyperfine components (HCN, N$_2$H$^+$, and CN) we derived the opacity using the hyperfine components fitting method of the CLASS package. For the CS and C^{34}S molecular transitions we derived numerically the opacity using

$$\frac{T_{MB}(C^{34}S)}{T_{MB}(CS)} = \frac{1 - \exp(-\tau)}{1 - \exp(-\tau\, r)}, \qquad (1)$$

where r is the CS to C^{34}S abundance ratio, assumed to be equal to the terrestrial value (22.5, Kim & Koo 2003). We found a high opacity toward Cores 14 and 48 for CS (2–1), 10.8 and 6.0 respectively, whose spectra show self-absorption (see Fig. 3). For Cores 40 and 109 we found lower opacities, τ=3.1 and 4.2 for CS (2–1) respectively. We assumed optically thin emission in C$_3$H$_2$, DCO$^+$, and N$_2$D$^+$ (2–1), the latter with only the main hyperfine component detected. This conservative assumption could not be true, so the column densities should be taken as lower limits. We also derived the molecular abundances with respect to H$_2$ (see Table 8), taking into account the resolution for each molecular transition

TABLE 6
Line parameters[a].

Molecular transition	Source	T_{MB} [b] (K)	$A \times \tau$ [c] (K)	$\int T_{MB} dv$ [b] (K km s^{-1})	v_{LSR} (km s^{-1})	Δv_{LSR} (km s^{-1})	τ [d]	Profile[e]
C$_3$H$_2$ (2$_{1,2}$–1$_{1,0}$)	Core 14	0.37(6)	-	0.086(11)	3.502(14)	0.22(3)	-	G
	Core 40	1.19(5)	-	0.347(9)	3.420(4)	0.273(9)	-	G
	Core 109	2.74(6)	-	0.799(13)	5.8340(20)	0.274(5)	-	G
CS (2–1)	Core 14	0.69(10)	-	0.41(3)	3.439(21)	0.45(4)	10.8(1.1)	SA
	Core 40	1.94(7)	-	0.560(17)	3.369(4)	0.415(14)	3.1(3)	NS
	Core 48	0.79(7)	-	0.402(18)	3.684(11)	0.477(22)	6.0(6)	SA
	Core 109	1.93(8)	-	0.743(17)	5.836(4)	0.361(9)	4.2(4)	G
C^{34}S (2–1)	Core 14	0.267(25)	-	0.068(5)	3.545(8)	0.241(20)	0.5(1)	G
	Core 40	0.268(16)	-	0.069(3)	3.381(5)	0.241(13)	0.14(1)	G
	Core 48	0.187(23)	-	0.041(4)	3.729(11)	0.20(3)	0.26(3)	G
	Core 109	0.34(3)	-	0.083(5)	5.825(7)	0.233(17)	0.19(2)	G
N$_2$D$^+$ (2–1) [f]	Core 40	0.084(20)	-	0.019(3)	3.280(15)	0.21(3)	-	G
	Core 109	0.31(4)	-	0.109(7)	5.673(11)	0.331(22)	-	G
DCO$^+$ (3–2)	Core 109	0.70(11)	-	0.151(18)	5.828(13)	0.202(21)	-	G
HCN (1–0)	Core 40	-	1.55(11)	-	3.410(16)	0.334(22)	6.0(5)	NS
	Core 48	-	0.33(10)	-	3.54(5)	0.90(11)	2.4(1.2)	G
	Core 109 (1)	-	2.53(3)	-	5.93(7)	0.16(22)	0.25(10)	NS
	Core 109 (2)	-	6.10(3)	-	5.72(7)	0.25(22)	10.20(10)	NS
N$_2$H$^+$ (1–0)	Core 14	-	0.0341(16)	-	11.500(5)	0.206(10)	0.10(9)	G
	Core 40	-	0.219(12)	-	11.4000(19)	0.249(5)	0.171(25)	G
	Core 109	-	0.904(14)	-	13.8000(5)	0.2150(11)	0.467(11)	G
CN (1–0)	Core 14	-	0.051(9)	-	3.64(8)	0.81(15)	0.1(7)	G
	Core 40	-	0.65(22)	-	3.430(21)	0.36(5)	3.9(1.3)	G
	Core 109 (1)	-	1.41(22)	-	5.930(5)	0.162(11)	1.13(23)	G
	Core 109 (2)	-	2.3(1.3)	-	5.670(7)	0.101(16)	4.(3)	G

(a) Line parameters of the detected lines. The former five molecular transitions have no hyperfine components. The parameters for the transitions labeled as G (see last column) have been derived from a Gaussian fit while line parameters of NS and SA profiles have been derived from the intensity peak (T_{MB}), and zero (integrated intensity), first (line velocity) and second (line width) order moments of the emission. The latter three molecular transitions have hyperfine components. The parameters have been derived using the hyperfine component fitting method of the CLASS package. The value in parenthesis shows the uncertainty of the last digit/s. If the two first significative digits of the error are smaller than 25, two digits are given to better constrain it.
(b) Only for molecular transitions with no hyperfine components.
(c) Only for molecular transitions with hyperfine components.
(d) Derived from a CLASS hyperfine fit for molecular transitions with hyperfine components. Derived numerically for CS and C^{34}S using Eq. 1. A value of 0.3 is assumed when no measurement is available.
(e) G: Gaussian profile. NS: Non-symmetric profile. SA: Self-absorption profile.
(f) Only the main component is detected.

(see Table 4).

4. DISCUSSION

We observed four selected cores located in the different regions of the Pipe Nebula (*bowl*, *stem*, and B59), in different molecular tracers and in dust continuum emission, to study and compare their physical and chemical properties. The cores were selected based on the results of the optical polarimetric survey carried out by Alves et al. (2008). In the following subsections, we discuss and compare the properties of each individual core, as well as an overall analysis of such properties, and we try to relate our results with previous works. In particular, in the next subsection we compare the dust continuum emission with the visual extinction maps of Rathborne et al. (2008) and the trend found for the diffuse gas by Alves et al. (2008).

4.1. *Comparison of visual extinction and 1.2 mm continuum emission maps*

The beam size of our observations is 11″, convolved to a Gaussian of 21.″5 in the maps shown (see §3.1), while that of Rathborne et al. (2008) is ~60″. Hence, our maps suffer from less beam dilution and we can resolve smaller structures. The sensitivity limit of the A_V observations is fixed at 1.2 mag (Lada et al. 2008), which corresponds to a column density of

~1×10^{21} cm^{-2} (Wagenblast & Hartquist 1989). A conservative estimation of the sensitivity limit of our maps, in the same conditions, can be derived using the 3-σ emission level of the noisiest continuum map convolved to a 60″ Gaussian. The resulting beam averaged column density, for a T_K of 10 K, is ~4×10^{20} cm^{-2}. Therefore, as seen from the minimum column densities in the same conditions, our dataset have slightly better sensitivity. Lada et al. (2008) defines the equivalent radius of the core using the region with emission brighter than 3-σ, while we use the region with emission brighter than half of the peak value. This difference prevents a direct comparison of the radii and densities. The core masses, however, depend only on the integrated flux density and can be compared. Our masses are on average ~3.4 times smaller, ranging from ~0.9 for Core 109 to ~7 for Core 14.

We estimated the difference between the 2MASS extinction maps (Lombardi et al. 2006) and the 1.2 mm dust maps. To do this we first transformed the original near-IR extinction maps to visual extinction maps using $A_V = A_k/0.118$ (Dutra et al. 2002). Then, we convolved the 1.2 mm dust maps with a Gaussian of 60″ to have the same resolution. We transformed the 1.2 mm dust maps to column density maps (see Appendix A for details). We assumed a uniform typical temperature of 10 K for all the cores. To estimate the uncertainty caused by this assumption, we also made
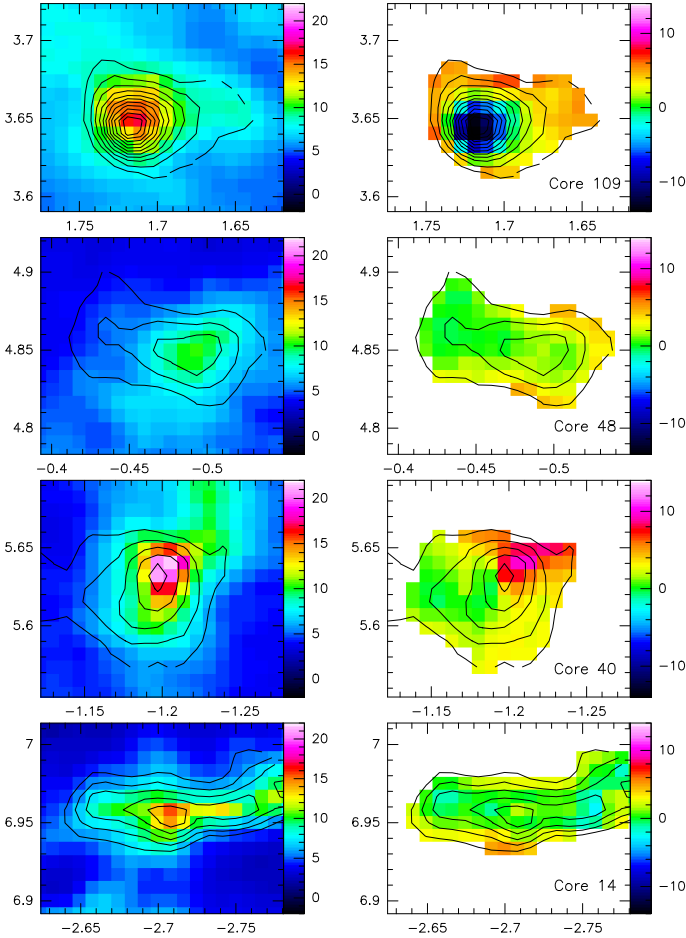
FIG. 5.— *Left panels*: Color image of the visual extinction map derived from the near-IR observations (Lombardi et al. 2006) superposed with the contour map of the extinction map derived from our 1.2 mm dust continuum maps in galactic coordinates. Contours are from 2.5 to 30 visual magnitudes by steps of 2.5. *Right panels*: Color image of the difference between the visual extinction map derived from the near-IR and the 1.2 mm observations within the region of the A_V converted dust continuum maps with A_V>2.5 magnitudes. Contours are the same as in the left panels. Core number is indicated in the lower right corner of the panels. The color scale (in visual magnitudes) are shown in the right side of the panels.

the calculations for temperatures of 8 and 12 K, which resulted in an average maximum variation over the whole map of ~2.4 extinction magnitudes. We also assumed for all the cores $\kappa_{250\ GHz}$=0.0066 cm^2 g^{-1} as average value between dust grains with thin and thick ice mantles for a volume density of ~10^5 cm^{-3} (Ossenkopf & Henning 1994) with an uncertainty of about a factor of 2. As a final step, we used the relationship $A_V = 1.258 \times 10^{-21} N_{H_2}$ (Wagenblast & Hartquist 1989) to transform column density to visual extinction. The resulting maps of the difference between the extinction maps derived from near-IR and mm data are shown in the right-hand side panels of Fig. 5. For Core 40 we found an excess of extinction that could be due to the filtered diffuse emission (see §3.1). However, in such a case, one would expect this excess to be present over the whole map. For Cores 14 and 48 we found a good agreement between both tracers. On the other hand, at denser regions such as the center of Core 109 (n_{H_2}>4×10^5 cm^{-3}), the A_V derived from the 1.2 mm dust is significantly larger, ≳10 mag, than that derived from the near-IR. This is the core with the highest column density (~4.8×10^{22} cm^{-2}), therefore this suggests that near-

IR extinction maps constructed from 2MASS catalogs do not have enough sensitivity or sampling scale to resolve the centers of very dense cores. In such dense regions, the number of 2MASS catalog background stars is not high enough to provide neither a large number of sources per pixel, nor a large number of high extinction measurements, thus the high extinction regions might be poorly resolved and underestimated. These biases may explain, combined with the larger radius, the lower densities reported by Rathborne et al. (2008). Extensive observations toward the Perseus cloud in visual extinction and in radio continuum provide similar results (Kirk et al. 2006). Extinction maps with higher resolution, made with deeper observations, are able to resolve better the high extinction levels. For example, Kandori et al. (2005) observed Core 109 (named FeSt 1-457) in A_V deeper with a resolution of ~30″, and found a morphology in perfect agreement with our continuum observations. Their A_V intensity peak at the core center of A_V~41.0 (the largest in their sample) is very close to our derivation, A_V~39.2, for a 30″ beam.

Summarizing, our dust continuum maps seem to be better at tracing the high extinction regions of the prestellar cores, at least at this spacial resolution. These results suggest that the dust continuum emission would trace the dense and cold cores better than the 2MASS derived visual extinction. On the other hand, the visual extinction would be more sensitive to the cloud diffuse extended emission.

4.2. *Discussion on the individual cores*
4.2.1. *Core 14*

Core 14, located in B59, is a compact and dense core but the less massive in our sample. It is the only core that belongs to a clumpy and filamentary structure, which is elongated along the NE-SW direction with an extent of ~500″ (~0.35 pc, see Fig. 2), with a morphology quite similar to that shown in A_V maps (Rathborne et al. 2008; Román-Zúñiga et al. 2009). The location of Core 14 inside an elongated and clumpy filament, suggests that probably it is still undergoing fragmentation, which could lead to the formation of smaller cores. In fact, it is resolved in several small clumps which have sizes comparable to the sizes of the other cores in the Pipe, with radii of about ~0.04 pc.

Core 14 shows emission in all the early-time molecules at 3 mm. CS (2–1) and C^{34}S (2–1) are clearly detected (see Fig. 3), and the abundances are the largest of the sample (see Table 8). On the other hand, C$_3$H$_2$ ($2_{1,2}$–$1_{1,0}$) and N$_2$H$^+$ (1–0) show weak emission and, consequently, low abundances. Rathborne et al. (2008) detect weak NH$_3$ emission, in good agreement with our N$_2$H$^+$ measurements. Only the main component of the CN (1–0) transitions is clearly detected. These are signatures of an object very young chemically.

4.2.2. *Core 40*

Core 40, located in the *stem*, is another core with irregular morphology. This core shows emission in all the transitions at 3 mm, of both early- and late-time molecules, and in the late-time N$_2$H$^+$ transition at 3 mm. The molecular emission of Core 40 is strong, and only the emission of Core 109 is more intense, except for CS, which shows the same T_{MB} for both cores. These cores are the only ones that show strong late-time molecule emission. Core 40 presents the highest CN and N$_2$H$^+$ abundances (see Table 8). Regarding N$_2$H$^+$, the intense emission with all the hyperfine components detected is in perfect agreement with previous results of NH$_3$ (Rathborne et al.

2008). The HCN emission for Core 40 is quite anomalous, because the main hyperfine component is weaker than the satellite components (see Fig. 4). This suggests that the emission is not in LTE. González-Alfonso & Cernicharo (1993) investigated with Monte-Carlo techniques the variation in HCN (1–0) profiles. According to their work, an infalling cloud with a dense central core (see Fig. 2) surrounded by a large diffuse envelope (Lombardi et al. 2006) may produce an HCN (1–0) spectrum as the observed toward Core 40.

4.2.3. *Core 48*

Core 48, located in the *stem*, has a quite elongated morphology. It is embedded in an environment with high polarization angle dispersion (Alves et al. 2008), which is the exception of this polarimetrically defined region. It is very diffuse, this is the largest and the less dense core in the sample. It shows emission only in three early-time molecules: CS (2–1), $C^{34}S$ (2–1) and, marginally, HCN (1–0). The abundances of CS and $C^{34}S$ are among the largest in the sample, slightly lower than those for Core 14. The N_2H^+ molecule was undetected, in agreement with previous measurements of NH_3 (Rathborne et al. 2008).

4.2.4. *Core 109*

Core 109, located in the *bowl*, is the most circular and compact core in the sample. The dust continuum emission of this core is similar to that of the other cores. However, it is the densest one in our sample and the most massive ($\sim 4\ M_\odot$). Kandori et al. (2005) find, through a Bonnor-Ebert profile fit, that Core 109 is gravitationally unstable. Aguti et al. (2007) find, through observations of molecular transitions, that this core (designated also as FeSt 1-457) is gravitationally bound. Kandori et al. (2005) suggest other models, apart from a Bonnor-Ebert sphere, including extra supporting mechanisms that might fit the density profile. Aguti et al. (2007) propose that Core 109 is pulsating, based on expansion motions of the outer layers. However, their Jeans mass measurement is compatible with the mass of the core and they propose a quasi-stable state near hydrodynamic equilibrium. This core is embedded in a magnetized medium (see § 4.4), thus, magnetic support could be a plausible source of external support.

This core shows emission of all the detected early- (C_3H_2, HCN, CS, $C^{34}S$, and CN) and late-time molecules (N_2H^+, N_2D^+ and DCO^+). The molecular emission of this core is always the strongest. Core 109 shows a very strong N_2H^+ emission, in agreement with the NH_3 measurements by Rathborne et al. (2008). As seen in Table 8, Core 109 has similar abundances for early-time molecules to those of the other cores. Interestingly, the CS and $C^{34}S$ abundances are the lowest in our sample, which suggests CS depletion toward the center (detected on $C^{18}O$, Aguti et al. 2007).

4.3. *Qualitative chemistry analysis*

Table 4 shows a variation of about a factor of ~ 4 around 10^{22} cm^{-2} of the average H_2 column densities derived for each of the cores with a 27″ beam, the one used to calculate the abundances for the molecular transitions at 3 mm. This represents, using the relationship $A_V = 6.289 \times 10^{-22} N_H$ (Wagenblast & Hartquist 1989), average values of $A_V \sim 4.4$ to ~ 19.4. The first case would represent a shallow core, more affected by the external radiation field, which tends to have a younger chemistry. The other extreme probably indicates a denser and more shielded core, where one would expect to find more complex and evolved molecules. However, note that this also depends on the time-scale needed to form the core (Tafalla et al. 2004; Crapsi et al. 2005).

We find that CS (see Table 8), an early-time molecule, is detected in all the cores with abundances with respect to H_2 of a few times 10^{-10}, similar to the ones found in other dense cores (Irvine et al. 1987) or the ones obtained in gas–phase chemical models (Taylor et al. 1998; Garrod et al. 2004). It is worth to mention that Cores 14 and 48 show high CS abundance, one order of magnitude higher than Cores 109 and 40. A similar result is found for the $C^{34}S$ abundances. The derived abundances for the early-time molecule HCN toward the cores in our sample is very uniform, and seems to be independent of their physical properties. The early-time molecule CN, a molecule that is also detected commonly in dense cores, has also a significantly lower abundance (a factor $\gtrsim 4$) toward Core 48 than toward the rest of the sample. Where detected, the CN abundance varies only within a factor of five. On the other hand, another early-time molecule such as C_3H_2, shows differences in abundances of at least a factor of five among Cores 14 and 48 with respect to Cores 40 and 109. Late-time molecules, such as N_2H^+ or deuterated molecules, are not broadly detected in our sample: N_2H^+ is detected except in Core 48. On the contrary, N_2D^+ is only detected on Cores 40 and 109, and DCO^+ only in Core 109. We found a higher abundance of N_2H^+ toward Core 40 than toward Core 109 by a factor of ~ 2, while Rathborne et al. (2008) found an abundance of NH_3 toward Core 109 higher than that of Core 40 by a factor of ~ 3.4. However, both Cores 40 and 109 show higher abundances in N_2H^+ than Cores 14 and 48. Despite Cores 14 and 40 having a similar average column density, the former shows 5 times less abundance of N_2H^+ than the latter. Moreover, Core 14 does not show emission in any other late-time molecule while Core 40 is detected in N_2D^+ showing an abundance only a factor of 4 lower than that of Core 109. Briefly, the higher abundances in Cores 109 and 40 with respect to Core 14 and in particular to Core 48 (except for CS) is an indication that Cores 109 and 40 are more chemically evolved than Cores 14 and 48. However, the molecular abundances of these two late-time species are roughly an order of magnitude lower than the prototypical starless cores L1517B and L1498 (Tafalla et al. 2006), which suggests that Cores 109 and 40 may be in an earlier evolutionary stage than cores in Taurus.

Rathborne et al. (2008) observed the emission of the NH_3 (1,1), NH_3 (2,2), CCS (2_1–1_0), and HC_5N (9–8) transitions towards 46 cores of the Pipe Nebula. Cores 14, 40, 48, and 109 were included in their observations. None of the lines were detected in Core 48, which is shown to be again the more chemically poor core of our sample. HC_5N was not detected in core 14, which also has the weakest CCS and NH_3 lines. The four transitions were detected in cores 40 and 109, but with some differences. The NH_3 lines are much more intense in core 109, a factor of ~ 4 for the (1,1) transition and ~ 9 for the (2,2) line, while the CCS line is more intense in core 40, less than a factor of ~ 2, and the HC_5N lines are very similar in both cores, inside the RMS. All these results are consistent with our observations: Core 48, which did not show emission of late-time molecules, is very poor chemically and shows a very young chemistry. Core 14, has some very weak emission of late-time molecules (NH_3) but only weak emission of CCS, an early-time molecule. Core 40 is more evolved chemically and shows stronger emission of early-time molecules than of late-time molecules. Finally, Core 109 is the one showing more diversity of molecules

TABLE 7
MOLECULAR COLUMN DENSITIES OF THE CHEMICAL SPECIES OBSERVED TOWARD THE PIPE NEBULA CORES IN CM^{-2}.

Source	C_3H_2 [a]	CS	$C^{34}S$	CN	HCN	N_2H^+	N_2D^+ [a]	DCO^+ [a]
Core 14	3.84×10^{11}	3.07×10^{13}	6.19×10^{11}	1.16×10^{12}	$< 5.42 \times 10^{10}$	9.70×10^{10}	$< 8.09 \times 10^{09}$	$< 5.13 \times 10^{11}$
Core 40	1.65×10^{12}	7.11×10^{12}	2.94×10^{11}	4.70×10^{12}	2.57×10^{12}	4.89×10^{11}	2.17×10^{09}	$< 4.93 \times 10^{10}$
Core 48	$< 7.93 \times 10^{10}$	1.53×10^{13}	2.94×10^{11}	$< 1.64 \times 10^{11}$	2.59×10^{12}	$< 3.79 \times 10^{10}$	$< 6.88 \times 10^{09}$	$< 7.82 \times 10^{10}$
Core 109	6.36×10^{12}	1.25×10^{13}	3.68×10^{11}	2.76×10^{12}	9.80×10^{12}	6.79×10^{11}	2.72×10^{10}	1.41×10^{11}

(a) Transition with no opacity mesurements available, thus optically thin emission is assumed to obtain lower limits of the column densities.

TABLE 8
ABUNDANCES[a] OF THE CHEMICAL SPECIES WITH RESPECT TO H$_2$ OBSERVED TOWARD THE PIPE NEBULA CORES.

Source	C_3H_2 [b]	CS	$C^{34}S$	CN	HCN	N_2H^+	N_2D^+ [a]	DCO^+ [a]
Core 14	3.45×10^{-11}	2.77×10^{-09}	5.58×10^{-11}	9.58×10^{-11}	$< 4.88 \times 10^{-12}$	8.73×10^{-12}	$< 5.84 \times 10^{-13}$	$< 2.93 \times 10^{-11}$
Core 40	1.55×10^{-10}	6.64×10^{-10}	2.75×10^{-11}	4.19×10^{-10}	2.41×10^{-10}	4.58×10^{-11}	1.69×10^{-13}	$< 3.73 \times 10^{-12}$
Core 48	$< 1.13 \times 10^{-11}$	2.19×10^{-09}	4.21×10^{-11}	$< 2.22 \times 10^{-11}$	3.71×10^{-10}	$< 5.43 \times 10^{-12}$	$< 7.75 \times 10^{-13}$	$< 7.17 \times 10^{-12}$
Core 109	2.06×10^{-10}	4.06×10^{-10}	1.19×10^{-11}	8.54×10^{-11}	3.18×10^{-10}	2.20×10^{-11}	7.30×10^{-13}	3.37×10^{-12}

(a) See Tables 4 and 7 for dust and line column densities.
(b) Transition with no opacity mesurements available, thus optically thin emission is assumed to estimate a lower limit of the column densities and, consequently, of the abundances.
(c) Due to the lack of C^{34}S data we assume optically thin emission to obtain a lower limit of the column density and, as a result, also for the abundance.

TABLE 9
PIPE NEBULA CORE GENERAL PROPERTIES WITH RESPECT TO CORE 109.

	Diameter (pc)	Mass ($M_\odot$)	N_{H_2} (10^{21}cm^{-2})	n_{H_2} (10^4cm^{-3})	$p_\%$ [a] (%)	δPA [a] (^{o})	$X(N_2H^+)$ (10^{-11})	$X(CN)$ (10^{-11})	$X(C_3H_2)$ (10^{-11})	$X(CS)$ (10^{-11})
Core 109	0.063	4.00	47.60	36.57	11.0	3.9	2.20	8.54	20.6	40.6

Relative values	Diameter	Mass	N_{H_2}	n_{H_2}	$p_\%$	δPA	$X(N_2H^+)$	$X(CN)$	$X(C_3H_2)$	$X(CS)$
Core 109	10.0	10.0	10.0	10.0	10.0	10.0	10.0	10.0	10.0	10.0
Core 40	16.5	6.3	2.3	1.4	4.2	22.2	20.8	49.1	7.5	16.4
Core 14	11.3	3.5	2.8	2.5	1.8	40.4	4.0	11.2	1.7	68.2
Core 48	20.2	5.2	1.3	0.6	1.8	83.8	<2.5	<2.6	<0.6	53.9

(a) Franco et al. (2010)

and the more intense emission, in particular of late-time molecules. Interestingly, the CCS abundance in core 109 is probably lower than in core 40, which is consistent with the view that the CCS molecule is destroyed soon after the formation of a dense core, probably as a result of the contraction of the core (de Gregorio-Monsalvo et al. 2006; Millar & Herbst 1990; Suzuki et al. 1992). This would reinforce the view that this core is in a very advanced evolutionary state.

In summary, Core 109 seems to be the more chemically evolved core, probably because it is more dense and because it shows higher abundances of late-time molecules. Core 40, with three times lower column density, also shows large N_2H^+ abundances. It might be in an intermediate chemical evolutionary stage. These two cores probably are in an evolutionary stage slightly younger than that of the prototypical starless cores (Tafalla et al. 2004; Crapsi et al. 2005). Cores 48 and 14 show similar physical properties in terms of size, mass and H$_2$ column density, to Cores 109 and 40. However, they appear to be very chemically poor and, therefore, they could be in an even younger stage of chemical evolution.

4.4. *Evolutionary trend and correlation with the diffuse gas*

Table 9 shows the summary of the main properties of the cores relative to Core 109, which is the one that shows the strongest line emission. In this table we show the physical and chemical properties. Additionally, we added the averaged polarimetric properties of the diffuse envelope around the cores (Alves et al. 2008; Franco et al. 2010): polarization fraction ($p_\%$) and dispersion of the polarization position angle (δPA).

As shown in Fig. 2, the polarization vectors calculated from optical extinction cannot be derived at the more dense regions, where the visual extinction is higher. In Fig. 2, except for the map of Core 48 with the lowest RMS, the polarization vectors lie in regions below the 3-σ noise level. However, the trend of the polarization vectors is in general rather uniform over the whole map. Indeed, there are vectors up to very close to the dense parts of the cores. Consequently, the derived magnetic field properties of the diffuse surrounding medium are also representative of those of the dense part of the cores.

A relationship between the magnetic and the chemical properties of each core seems to exist. The two more chemically evolved cores, 109 and 40, appear to be embedded in a strongly magnetized environment, as δPA values clearly reflect (see Table 9). The other two cores, 14 and 48, do not show very different morphological properties with respect to the previous two (size and mass). However, their chemical properties are completely opposed, and they are likely younger cores in chemical time-scale. Interestingly, the magnetic properties of Cores 14 and 48 are also opposed to those of Cores 40 and 109. Cores 14 and 48 are surrounded by a molecular diffuse medium that is much more turbulent than that surrounding the two previous ones. Core 14 is possibly affected by the star formation undergoing in the nearby region

B59. Core 48 appears to be dominated by turbulence and constitutes an exception in the *stem*, whose cores have uniform magnetic properties among them, showing low $p_{\%}$ and high δPA (Franco et al. 2010).

In summary, these four cores of the Pipe Nebula have similar masses and sizes, but they are in different stages of chemical evolution: Cores 109 and 40 are much more evolved chemically than Cores 48 and 14. The different magnetic properties of the diffuse molecular environment suggest that Cores 109 and 40 have grown in a more quiescent and slowly way (probably through ambipolar diffusion), whereas the growth of Cores 14 and 48 has occurred much faster, an indication that possibly a compression wave that generates turbulence or the turbulence itself (Falle & Hartquist 2002; Ballesteros-Paredes et al. 2007). The longer time–scale of the ambipolar diffusion process could explain the more evolved chemistry found toward the cores surrounded by a magnetized medium. These features suggest two different formation scenarios depending on the balance between turbulent and magnetic energy in the surrounding environment. The importance of these results is worth of a more detailed study of the Pipe Nebula cores in order to fully confirm these trends.

5. SUMMARY AND CONCLUSIONS

We carried out observations of continuum and line emission toward four starless cores of the Pipe Nebula spread out along the whole cloud selected in base of their magnetic properties (Alves et al. 2008; Franco et al. 2010). We studied their physical and chemical properties, and the correlation with the magnetic field properties of the surrounding diffuse gas.

1. The dust continuum emission of the observed Pipe Nebula cores shows quite different morphologies. In the sample there are diffuse cores, such as Cores 40 and 48, and compact and dense cores, such as Core 109. We have also mapped a clumpy filament, which contains the embedded Core 14. This filament is possibly undergoing fragmentation into smaller cores of sizes comparable to that of the others. We derived average radii of ~0.09 pc (~18600 AU), densities of ~1.3×10^5 cm^{-3}, and core masses of ~2.5 $M_\odot$.

2. The dust continuum peak coincides within the errors with A_V peak derived from the 2MASS catalog. The continuum emission is more sensitive toward the dense regions, up to $\gtrsim 10$ magnitudes for the densest cores. On the other hand, the diffuse emission is better traced by the extinction maps. The masses are in average ~3.4 times smaller.

3. We have observed several early- and late-time lines of molecular emission toward the cores and derived their column densities and abundances. The starless cores of the Pipe Nebula are all very young, but they present different chemical properties possibly related to a different evolutionary stage. However, there does not seem to be a clear correlation between the chemical evolutionary stage of the cores and their position in the cloud. Cores 109 and 40 show late-time molecular emission and seem to be more chemically evolved. Core 109 shows high abundances of late-time molecules and it seems to be the more chemically evolved. Core 40 has three times lower H$_2$ column density than that of Core 109. It presents a large N$_2$H$^+$ abundance and the largest CN abundance, thus it might be in an intermediate chemical evolutionary stage. Cores 48 and 14 show only early-time molecular emission, and Core 14 presents weak N$_2$H$^+$ emission, and seem to be chemically younger than the other two cores. Core 14 has a similar mass and size than Core 40, but the N$_2$H$^+$, C$_3$H$_2$, and CS abundances are about one order of magnitude lower than the Core 40 abundances. Our results and interpretation of the evolutionary stage of each core are consistent with the previous observations of Rathborne et al. (2008) in these same cores.

4. There seems to be a relationship between the properties of the magnetic field in the cloud medium of the cores and the chemical evolutionary stage of the cores themselves. The two more chemically evolved cores, 109 and 40, appear to be embedded in a strongly magnetized environment, with a turbulent to magnetic energy ratio of 0.05 and 0.27, respectively. The two chemically younger cores, 14 and 48, appear to be embedded in a more turbulent medium. This suggests that the magnetized cores probably grow in a more quiescent way, probably through ambipolar diffusion, in a time-scale large enough to develop the richer chemistry found. On the other hand, the less magnetized cores likely grow much faster, probably in a turbulence dominated process, in a time-scale too short to develop late-time chemistry.

5. The Pipe Nebula has revealed to be an excellent laboratory for the study of the very early stages of the star formation. The studied cores show different morphologies, chemical evolutionary stages and magnetic properties. The physical and chemical properties are not directly linked as the competition between the magnetic field and turbulence at small scales seems to have an important influence in the core evolution. The importance of these results require a more detailed study of the chemistry and magnetic field properties of the cores to fully confirm these results.

REFERENCES

Aguti, E. D., Lada, C. J., Bergin, E. A., Alves, J. F., & Birkinshaw, M. 2007, ApJ, 665, 457

Aikawa, Y., Ohashi, N., & Herbst, E. 2003, ApJ, 593, 906
Aikawa, Y., Wakelam, V., Garrod, R. T., Herbst, E. 2008, ApJ, 674, 984

Alves, F. O. & Franco, G. A. P. 2007, A&A, 470, 597

Alves, F. O., Franco, G. A. P., & Girart, J. M. 2008, A&A, 486, L13

Ballesteros-Paredes, J., Klessen, R. S., Mac Low, M.-M., & Vazquez-Semadeni, E. 2007, Protostars and Planets V, 63

Bergin, E. A., Ciardi, D. R., Lada, C. J., Alves, J., Lada, E. A. 2001, ApJ, 557, 209-225

Bergin, E. A. & Tafalla, M. 2007, ARA&A, 45, 339

Brooke, T., Huard, T. L., Bourke, T. L., Boogert, A. C. A. et al. 2007, ApJ, 655, 364

Caselli, P., Benson, P. J., Myers, P. C., Tafalla, M. 2002, ApJ, 572, 238

Crapsi, A., Caselli, P., Walmsley, C. M., Myers, P. C., Tafalla, M., Lee, C. W., Bourke, T. L. 2005, ApJ, 619, 379

Dutra, C. M., Santiago, B. X., Bica, E. 2002, A&A, 381, 219

Falle, S. A. E. G., & Hartquist, T. W. 2002, MNRAS, 329, 195

Franco, G. A. P., Alves, F. O., & Girart, J. M. 2010, ApJ, accepted (arXiv:1008:5327v2)

Flower, D. R., Pineau Des Forêts, G., Walmsley, C. M. 2006, A&A, 456, 215

Forbrich, J., Lada, C. J., Muench, A. A., Alves, J., Lombardi, M. 2009, ApJ, 704, 292

Garrod, R. T., Williams, D. A., Hartquist, T. W., Rawlings, J. M. C., Viti, S. 2004, MNRAS, 356, 654-664

González-Alfonso, E. & Cernicharo, J. 1993, A&A, 279, 506

de Gregorio-Monsalvo, I., Gómes, J. F., Suárez, O., Kuiper, T. B. H., Rodríguez, L. F., Jiménez-Bailón, E. 2006, ApJ, 642, 319

Irvine, W. M., Goldsmith, P. F., Hjalmarson A. 1987, in Hollenbach D. J., Thronson H. A. (eds), Interstellar Processes. Reidel, Dordrecht, p. 561

Kandori, R., Nakajima, Y., Tamura, M., Tatematsu, K., Aikawa, Y., Naoi, T., Sugitani, K., Nakaya, H., Nagayama, T., Nagata, T., Kurita, M., Kato, D., Nagashima, C., Sato, S. 2005, AJ, 130, 2166

Kauffmann, J., Bertoldi, F., Bourke, T. L., Evans, N. J., II, & Lee, C. W. 2008, A&A, 487, 993

Kim, K.-T., & Koo, B.-C. 2003, ApJ, 596, 362

Kontinen, S., Harju, J., Heikkilä, A., & Haikala, L. K. 2000, A&A, 361, 704

Lada, C. J., Muench, A. A., Rathborne, J. M., Alves, J. F., & Lombardi, M. 2008, ApJ, 672, 410

Lombardi, M., Alves, J., & Lada, C. J. 2006, A&A, 454, 781

Millar, T., Herbst, E. 1990, A&A, 231, 466

Morata, O., Girart, J. M., Estalella, R. 2003, A&A, 397, 181

Morata, O., Girart, J. M., & Estalella, R. 2005, A&A, 435, 113

Muench, A. A., Lada, C. J., Rathborne, J. M., Alves, J. F., & Lombardi, M. 2007, ApJ, 671, 1820

Ohashi, N., Lee, S. W., Wilner, D. J., Hayashi, M. 1999, ApJ, 518, L41

Onishi, T., Kawamura, A., Abe, R., Yamaguchi, N. et al. 1999, PASJ, 51, 871

Ossenkopf, V. & Henning, T. 1994, A&A, 291, 943

Rathborne, J. M., Lada, C. J., Muench, A. A., Alves, J. F., & Lombardi, M. 2008, ApJS, 174, 396

Román-Zúñiga, C., Lada, C. J., & Alves, J. F. 2009, ApJ, 704, 183

Suzuki, H., Yamamoto, S., Ohishi, M., Kaifu, N., Ishikawa, S., Hirahara, Y., Takano, S. 1992, ApJ, 392, 551

Tafalla, M., Myers, P. C., Caselli, P., Walmsley, C. M., & Comito, C. 2002, ApJ, 569, 815

Tafalla, M., Myers, P. C., Caselli, P., Walmsley, C. 2004, A&A, 416, 191

Tafalla, M., Santiago-García, J., Myers, P. C., Caselli, P., Walmsley, C. M., Crapsi, A. 2006, A&A, 455, 577

Taylor, S. D., Morata, O., Williams, D. A. 1998, A&A, 336, 309

Wagenblast, R., Hartquist, T. W., 1989, MNRAS, 237, 1019

APPENDIX

A. CALCULATION OF COLUMN DENSITY AND MASS OF DUST EMISSION

Radiative transfer equation and Planck function

The intensity emitted by an assumed homogeneous medium of temperature T_{ex} and optical depth τ_ν at frequency ν is given by

$$I_\nu = B_\nu(T_{ex})\left(1 - e^{-\tau_\nu}\right),\tag{A1}$$

where B_ν is the Planck function,

$$B_\nu = \frac{2h\nu^3}{c^2}\frac{1}{e^{h\nu/kT} - 1},\tag{A2}$$

and c is the speed of light, k the Boltzmann's constant and h the Planck's constant. The Rayleigh-Jeans limit, $h\nu \ll kT$ (in practical units $[\nu/\mathrm{GHz}] \ll 20.8\,[T/\mathrm{K}]$), does not hold for MAMBO-II observations (250GHz) of prestellar cores ($T \simeq 10$K), preventing the use of this limit simplification.

Telescope measurements

The beam solid angle is $\Omega_A = \int_{\mathrm{beam}} P d\Omega$, where P is the normalized power pattern of the telescope. Assuming that the telescope has a gaussian beam profile, P reads $P(\theta) = \exp(-4\ln 2\,\theta^2/\theta^2_{\mathrm{HPBW}})$, where θ is the angular distance from the beam center. The beam solid angle is

$$\Omega_A = \frac{\pi}{4\ln(2)}\theta^2_{\mathrm{HPBW}}.\tag{A3}$$

For discrete sources we measure flux densities, S_ν, instead of intensities, I_ν. These two quantities are related by

$$S_\nu = \int_{\mathrm{source}} I_\nu\, P\, d\Omega.\tag{A4}$$

This integration for a beam area, S_ν^{beam}, allows us to calculate the beam-averaged intensity as

$$\langle I_\nu \rangle = \frac{S_\nu^{\mathrm{beam}}}{\Omega_A}.\tag{A5}$$

From Flux to Column Density and Mass

One can calculate the opacity of the emission measured inside a beam, τ_ν^{beam}, from equations A1 and A5, relating it with the measured flux by

$$\tau_\nu^{\mathrm{beam}} = -\ln\left(1 - \frac{S_\nu^{\mathrm{beam}}}{\Omega_A\, B_\nu(T)}\right).\tag{A6}$$

On the other hand, the optical depth is defined as

$$\tau_\nu \equiv \int_{\mathrm{line\ of\ sight}} \kappa_\nu \rho\, ds,\tag{A7}$$

where κ_ν is the absorption coefficient per unit density.

One can relate the column density with the optical depth and, thus, with the measured flux using

$$N_{\mathrm{H}_2} = \int n_{\mathrm{H}_2}\, ds = \int \frac{\rho}{\mu\, m_{\mathrm{H}}} ds = \frac{\tau_\nu}{\mu\, m_{\mathrm{H}}\, \kappa_\nu},\tag{A8}$$

which particularized to a beam is $N_{\mathrm{H}_2}^{\mathrm{beam}} = \frac{\tau_\nu^{\mathrm{beam}}}{\mu\, m_{\mathrm{H}}\, \kappa_\nu}$,, where m_{H} is the hydrogen mass and μ is the mean molecular mass per hydrogen atom. In the case of optically thin emission the intensity is proportional to the column density as Eq. A1 can be simplified to $I_\nu \approx B_\nu(T)\tau_\nu$.

Then, the mass can be calculated as

$$M = \mu\, m_{\mathrm{H}}\, D^2 \int N_{\mathrm{H}_2}\, d\Omega,\tag{A9}$$

which for a beam is $M^{\mathrm{beam}} = \mu\, m_{\mathrm{H}}\, D^2\, N_{\mathrm{H}_2}^{\mathrm{beam}}\, \Omega_A$, where D is the distance to the source. All these calculations can be applied to any solid angle bigger than a beam.

B. CALCULATION OF COLUMN DENSITY OF LINE EMISSION

The column density for a $J \rightarrow J-1$ transition of a molecule ('Mol') is

$$N_{\text{Mol}} = \frac{3\,k}{8\pi^3} \frac{Q_{\text{rot}}}{g_K\,g_I} \frac{e^{Eu/T_{\text{ex}}}}{\nu} \frac{1}{S_{JkI}\,\mu^2} \frac{J_\nu(T_{\text{ex}})}{J_\nu(T_{\text{ex}}) - J_\nu(T_{\text{bg}})} \frac{\tau}{1 - e^{-\tau}} \int_{\text{line}} T_{\text{MB}}\,d\text{v}, \tag{B1}$$

which translates into useful units as

$$\left[\frac{N_{\text{Mol}}}{\text{cm}^{-2}}\right] = 1.67 \times 10^{14} \frac{Q_{\text{rot}}}{g_K\,g_I} \left[\frac{S_{JkI}}{\text{erg cm}^3\,\text{statC}^{-2}\,\text{cm}^{-2}}\right]^{-1} \left[\frac{\mu}{\text{D}}\right]^{-2} e^{Eu/T_{\text{ex}}} \left[\frac{\nu}{\text{GHz}}\right]^{-1} \frac{J_\nu(T_{\text{ex}})}{J_\nu(T_{\text{ex}}) - J_\nu(T_{\text{bg}})} \frac{\tau}{1 - e^{-\tau}} \left[\frac{\int_{\text{line}} T_{\text{MB}}\,d\text{v}}{\text{K km s}^{-1}}\right]. \tag{B2}$$

Here, J_ν is the energy in units of temperature, and it reads $J_\nu(T) = \frac{h\nu/k}{e^{h\nu/kT}-1}$. See next subsections for a detailed description of all the terms involved.

Observational terms

Single transitions

In case of single transitions, we have performed a Gaussian fit to the spectrum or a statistical moment calculation, both using tasks from the CLASS package. We obtain from either analysis the main beam temperature, T_{MB}, the line velocity, v, and the integrated emission, $\int T_{\text{MB}}\,d\text{v}$.

The opacity, τ, is calculated numerically in those molecules with more than one transition observed. In the other cases we have assumed $\tau \sim 0.3$. The excitation temperature, T_{ex}, can be calculated from the radiative transfer equation as

$$T_{\text{ex}} = \frac{h\nu}{k} \left[\ln\left(\frac{h\nu/k}{\frac{T_{\text{MB}}}{1-e^{-\tau}} + J_\nu(T_{\text{bg}})} + 1\right)\right]^{-1}, \tag{B3}$$

where T_{bg} is the background temperature.

Hyperfine transitions

In case of hyperfine transitions, we take into account all the hyperfine components of the selected transition. We have performed a hyperfine fit using CLASS, which provides $A \times \tau_m$, $\text{v}_{\text{LSR}}^{\text{reference line}}$, Δv, τ_m, where A is

$$A = f\left(J_\nu(T_{\text{ex}}) - J_\nu(T_{\text{bg}})\right), \tag{B4}$$

beeing f is the filling factor assumed to be ~ 1.

To be able to use equation B2 as in the single transition case, we need T_{ex}, τ and $\int T_{\text{MB}}\,d\text{v}$. We can calculate T_{ex} as in equation B3 calculating T_{MB} as $A \times \tau_m/\tau_m$, and τ_m is given by CLASS. For the integrated emission, we can use

$$\tau_0\,\Delta\text{v} = \int_{\text{line}} \tau\,d\text{v} \simeq \frac{1}{J_\nu(T_{\text{ex}}) - J_\nu(T_{\text{bg}})} \frac{\tau_0}{1 - e^{-\tau_0}} \int_{\text{line}} T_{\text{MB}}(\text{v})\,d\text{v}, \tag{B5}$$

leading to

$$\int_{\text{line}} T_{\text{MB}}(\text{v})\,d\text{v} \simeq \tau_0\,\Delta\text{v}\left(J_\nu(T_{\text{ex}}) - J_\nu(T_{\text{bg}})\right) \frac{1 - e^{-\tau_0}}{\tau_0}. \tag{B6}$$

Making this transformations eq. B2 can be used for hyperfine transitions.

Non-observational terms

Partition function (Q_{rot})

The rotational partition function, $Q_{\text{rot}}(T)$, is defined as

$$Q_{\text{rot}}(T) \equiv \sum g_J\,g_k\,g_I\,e^{-hBJ(J+1)/kT}, \tag{B7}$$

where the g_X factors are the degeneration of the respective quantic number, in particular $g_J = 2J + 1$.

Eq. B7 can be approximated, in the limit of high temperatures, by an integral because generally the energy levels are close together. We are only interested in the high temperature limit because is when the transition is activated, so this limit is accurate enough.

• **Linear molecules:** The solution for the diatomic case is general for any lineal molecule, so long as the molecular moment of inertia is computed properly for more than 2 atoms.

For lineal molecules $g_k = 1$, $g_I = 1$ and $g_J = (2J + 1)/\sigma$. σ (the symmetry number) is 1 for heteronuclear diatomic (C-O) or asymmetric linear polyatomic (O-N-N) molecules, and 2 for homonuclear diatomic (H-H) or symmetric linear polyatomic (O-C-O) molecules.

The partition function at high temperatures can be calculated as

$$Q_{\text{rot}} \simeq \frac{1}{\sigma} \int_0^\infty (2J + 1)e^{-hBJ(J+1)/kT}dJ \simeq \frac{1}{\sigma} \int_0^\infty e^{-(J^2+J)hB/kT}d(J^2 + J)) \simeq \frac{1}{\sigma}\frac{kT}{hB}, \tag{B8}$$

where B is the rotational constant available at the catalogues. A more accurate expression (Pickett et al., 2002) used in this work is

$$Q_{\text{rot}} \approx \frac{1}{\sigma}\left(\frac{kT}{hB} + \frac{1}{3} + \frac{1}{15}\frac{\sigma hB}{kT} + ...\right). \tag{B9}$$

• **Non-linear molecules:** Non-linear molecules have up to three moments of inertia and, thus, three rotational constants (A, B, C). In a similar way than before, but more complicated, the calculation of the rotational partition function at high temperatures is

$$Q_{\text{rot}} \approx \frac{\sqrt{\pi}}{\sigma}\left(\frac{KT}{h}\right)^{3/2}\frac{1}{\sqrt{ABC}}. \tag{B10}$$

Upper level energy (E_u)

We can calculate the energy of the upper level (E_u) as a function of the lower level (E_l) plus the energy of the photon emitted (both available at catalogues). This is, in units of temperature and using the units given in the catalogues,

$$\left[\frac{E_u}{K}\right] = 1.4388\left[\frac{E_l}{\text{cm}^{-1}}\right] + 4.799 \times 10^{-5}\left[\frac{\nu}{\text{MHz}}\right]. \tag{B11}$$

Intrinsic line strength times squared dipolar momentum ($S\,\mu^2$)

We can calculate the product of the *intrinsic* line strength, S_{JkI}, and the squared dipolar momentum, μ^2, from the Q_{rot} at 300 K (Q_{rot}^{300}), the line strength (LogINT) at 300 K and the lower state energy (E_l). All these parameters are available at the catalogues.

In a usable form,

$$\left[\frac{S\mu^2}{\text{erg cm}^3\,\text{statC}^{-2}\,\text{cm}^{-2}\,\text{D}^{-2}}\right] = 24025 \times \left[\frac{10^{LogINT}}{\text{MHz nm}^2}\right]Q_{\text{rot}}^{300}\left[\frac{\nu}{\text{MHz}}\right]^{-1}\left(\exp\left\{4.796 \times 10^{-3}\left[\frac{E_l}{\text{cm}^{-1}}\right]\right\}\right)\left(1 - \exp\left\{-1.6 \times 10^{-7}\left[\frac{\nu}{\text{MHz}}\right]\right\}\right)^{-1}. \tag{B12}$$